

Sommerfeld-Bethe analysis of ZT in inhomogeneous thermoelectrics

Manaho Matsubara^{1*}, Takahiro Yamamoto^{1,2} and Hidetoshi Fukuyama²

¹*Department of Physics, Faculty of Science, Tokyo University of Science, Shinjuku, Tokyo 162-8601, Japan*

²*Research Institute for Science and Technology, Tokyo University of Science, Shinjuku, Tokyo 162-8601, Japan*

The development of good thermoelectric materials exhibiting high ZT ($=\frac{PF}{\kappa}T$) requires maximizing power factor, PF , mainly governed by electrons, and minimizing thermal conductivity, κ , associated not only with electrons but also with phonons. In the present work, we focus on the GeTe and Mg_3Sb_2 as high ZT materials with inhomogeneous structures and analyze both electrical conductivity, L_{11} , and Seebeck coefficient, S , with help of Sommerfeld-Bethe formula, resulting in understanding the temperature dependence of PF and the identification of electrons contribution to thermal conductivity, κ_{el} . Comparing the obtained κ_{el} and experimentally measured κ , the temperature dependence of phonons contribution to thermal conductivity, $\kappa_{\text{ph}} = \kappa - \kappa_{\text{el}}$, is inferred and analyzed based on the formula by Holland. Comparison of the GeTe and Mg_3Sb_2 with different types of crystal structures, i.e., GeTe being of a semiordered zigzag nanostructure like a disrupted herringbone structure while Mg_3Sb_2 of rather uniform amorphous structure, discloses that size effects on temperature dependence of κ_{ph} is large in the former, while very small in the latter. Hence, it is concluded that not only the size of the grain but also its shape has an important influence on κ_{ph} and then ZT .

1. Introduction

In order to develop effective thermoelectric materials suitable to versatile conditions one needs solid scientific understanding based on electronic states as seen in the history of semiconductor technology. For such efforts, it is expected that detailed theoretical analysis of experiments demonstrating particular features with high values of figures of merit, PF (power factor) and ZT , will be useful since results of findings will lead to identification of important factors for the further development of good thermoelectrics. Here the basic theoretical

*mmatsubara@rs.tus.ac.jp

framework for this analysis is Kubo-Luttinger theory for thermoelectricity,^{1,2)} which gives electrical conductivity, L_{11} , thermoelectrical conductivity, L_{12} , electrothermal conductivity, L_{21} , and thermal conductivity (for zero electric field), L_{22} , by correlation functions between current density, J_{el} and thermal current density, J_{th} , respectively,

$$L_{11} : \int_0^\beta d\tau \langle T_\tau \{ J_{\text{el}}(\tau) J_{\text{el}}(0) \} \rangle e^{i\omega\lambda\tau}, \quad (1)$$

$$L_{12} = L_{21} : \int_0^\beta d\tau \langle T_\tau \{ J_{\text{el}}(\tau) J_{\text{th}}(0) \} \rangle e^{i\omega\lambda\tau}, \quad (2)$$

$$L_{22} : \int_0^\beta d\tau \langle T_\tau \{ J_{\text{th}}(\tau) J_{\text{th}}(0) \} \rangle e^{i\omega\lambda\tau}. \quad (3)$$

In terms of these L_{ij} , PF and ZT are given by

$$PF = \frac{1}{T^2} \frac{L_{12}^2}{L_{11}}, \quad (4)$$

and

$$ZT = \frac{PF}{\kappa} T, \quad (5)$$

respectively, and $\kappa = \left(L_{22} - \frac{L_{12}L_{21}}{L_{11}} \right) \frac{1}{T}$ is thermal conductivity (for zero electric current) consisting of two different sources, electrons κ_{el} and phonons κ_{ph} . (Possible contributions to κ by drag effects between electrons and phonons are included in κ_{ph} , though they are expected to be small in general cases because of the necessity of extra coupling between them.) Each of L_{ij} can be assessed with the help of thermal Green functions. Regarding PF , which is mainly governed by electrons, we have recently analyzed the remarkable experimental finding of large PF by Shimizu et al.³⁾ in high-quality FeSe thin films resulting in the proposal that the interplay between two two-dimensional bands nearby located in energy, one with the Fermi level leading large L_{11} while the other above the Fermi level contributing to a large value of Seebeck coefficient, $S = L_{12}/(TL_{11})$, as in semiconductors.⁴⁾ Incidentally, a similar possibility was pointed out by Uematsu et al. through studies on interfaces of GaAs.⁵⁾

In this paper, we address ZT where the interplay between electrons and phonons is crucial, which is not present in PF . Examples we study in this paper are GeTe⁶⁾ and Mg₃Sb₂,⁷⁾ both of which demonstrate high ZT , reflecting low κ , and share similar features of highly inhomogeneous structures, but show the different relation between such structures and κ , i.e., κ is sensitive to changes in defect structure in GeTe, but insensitive to changes in grain size in Mg₃Sb₂.

We first analyze PF which results in possible values of spectral conductivity, α , in L_{11} and L_{12} with the help of Sommerfeld-Bethe (SB) equations.⁸⁾ The α , thus determined, leads

naturally to identification of the electronic contribution to thermal conductivity, κ_{el} . By comparison with experimentally observed κ , phonon thermal conductivity, κ_{ph} , can be identified by $\kappa_{\text{ph}} = \kappa - \kappa_{\text{el}}$. The magnitude and the T dependences of κ_{ph} yield information of the long-wave length acoustic (LA) modes. The results indicate the damping of LA modes is sensitive to the types of morphology, e.g., shapes and spatial extent of grain boundaries. This identification of properties of phonons will lead to further explorations of choices of materials and processes governing morphology.

Cases of GeTe and Mg_3Sb_2 -based compounds are studied separately in Secs. 2 and 3, respectively, and the comparison of these two cases is given in Sec. 4, which is summarized in Sec. 5.

2. Case of GeTe

2.1 Electronic states and model of spectral conductivity

The pristine GeTe is rhombohedral and carriers (holes) are located in 6 valleys with average effective mass $m^* = 0.25m_0$ (m_0 is free electron mass).⁹⁾ L_{11} , L_{12} , and L_{22}^{el} (electron contribution to L_{22}), can be expressed by the SB relation as follows,^{8,10,11)}

$$L_{11} = \int_{-\infty}^{\infty} d\varepsilon \left(-\frac{\partial f(\varepsilon - \mu)}{\partial \varepsilon} \right) \alpha(\varepsilon), \quad (6)$$

$$L_{12} = -\frac{1}{e} \int_{-\infty}^{\infty} d\varepsilon \left(-\frac{\partial f(\varepsilon - \mu)}{\partial \varepsilon} \right) (\varepsilon - \mu) \alpha(\varepsilon), \quad (7)$$

$$L_{22}^{\text{el}} = \frac{1}{e^2} \int_{-\infty}^{\infty} d\varepsilon \left(-\frac{\partial f(\varepsilon - \mu)}{\partial \varepsilon} \right) (\varepsilon - \mu)^2 \alpha(\varepsilon), \quad (8)$$

where $f(\varepsilon - \mu) = 1/(\exp((\varepsilon - \mu)/k_B T) + 1)$ is the Fermi-Dirac distribution function with the chemical potential, μ , and the spectral conductivity, $\alpha(\varepsilon)$, is given as^{11,12)}

$$\alpha(\varepsilon, T) = g_s g_v \frac{\hbar}{2\pi V} \sum_{\mathbf{k}} \text{ReTr} \left[j_x(\mathbf{k}) G^{\text{A}}(\mathbf{k}, \varepsilon) j_x(\mathbf{k}) G^{\text{R}}(\mathbf{k}, \varepsilon) - j_x(\mathbf{k}) G^{\text{A}}(\mathbf{k}, \varepsilon) j_x(\mathbf{k}) G^{\text{R}}(\mathbf{k}, \varepsilon) \right]. \quad (9)$$

Here, $g_s (= 2)$ and $g_v (= 6)$ are the spin and valley degrees of freedom, respectively, V is the system volume, $j_x(\mathbf{k})$ is the current density in the x -direction along the T gradient of the material, and $G^{\text{R/A}}(\mathbf{k}, \varepsilon)$ is the retarded/advanced Green's functions. Within the effective mass approximation and the constant- τ approximation, $G^{\text{R/A}}(\mathbf{k}, \varepsilon)$ is represented as

$$G^{\text{R/A}}(\mathbf{k}, \varepsilon) = \frac{1}{\varepsilon - \frac{\hbar^2 k^2}{2m^*} \pm i\Gamma}, \quad (10)$$

where Γ is the scattering rate, and thus $\alpha(\varepsilon)$ is rewritten as

$$\alpha(\varepsilon) = g_s g_v \frac{e^2 \sqrt{m^*} \left(\sqrt{\varepsilon^2 + \Gamma^2} + |\varepsilon| \right)^{3/2}}{12\pi^2 \hbar^2 \Gamma}, \quad (11)$$

where e is the elementary charge and the energy origin is set at the band edge in a clean system. The Γ is assumed to be given by Matthiessen rule,¹³⁾ $\Gamma(T) = \Gamma_{\text{imp}} + \Gamma_{\text{el-ph}}(T)$, where Γ_{imp} is due to impurity scattering and $\Gamma_{\text{el-ph}}(T)$ is the phonons scattering at the high- T , $\Gamma_{\text{el-ph}}(T) = \gamma_{\text{el-ph}} T$.

2.2 Parameter-fitting for L_{11} , S , PF and electronic contributions to ZT

L_{11} , S and PF of both for pristine GeTe and doped GeTe ($\text{Ge}_{0.87}\text{Y}_{0.02}\text{Sb}_{0.10}\text{Ag}_{0.01}\text{Te}$), hereafter written as A_p and A_d , respectively, are shown in Fig. 1, where circles and squares are experimental data⁶⁾ and lines are results of model fitting with parameters given in Table I, with l_{el} being the mean free path of electrons at $T = 300$ K deduced by $l_{\text{el}} = \frac{\hbar}{\Gamma} \sqrt{\frac{\mu}{2m^*}}$.

Table I. Fitting parameters of GeTe-based compounds for L_{11} , S and PF , and l_{el} at $T = 300$ K.

	Pristine GeTe (A_p)	$\text{Ge}_{0.87}\text{Y}_{0.02}\text{Sb}_{0.10}\text{Ag}_{0.01}\text{Te}$ (A_d)
μ (eV)	$\varepsilon_F + 82.2 (k_B T)^2$	$\varepsilon_F + 42.0 (k_B T)^2$
ε_F (eV)	-3.9×10^{-1}	-9.8×10^{-2}
Γ_{imp} (eV)	2.0×10^{-2}	2.6×10^{-2}
$\gamma_{\text{el-ph}}$ (eV/K)	4.2×10^{-5}	2.6×10^{-6}
l_{el} (nm)	7	4

The Fermi energy ε_F of A_p and A_d shown in Table I are consistent with the experimental data⁶⁾ in view of the fact that the number of holes decreases by doping of the electrons from Y and Sb. As seen in Figs. 1(a) and 1(b), L_{11} is smaller and S is larger in A_d than those in A_p , reflecting the difference in the number of carriers. The results of parameter fitting, Γ_{imp} and $\gamma_{\text{el-ph}}$, are very reasonable: regarding Γ_{imp} it is natural that the impurity scattering gets stronger in doped case, A_d , with more planar defects and finer domain structures, whereas a possible explanation of new finding of weaker phonon scattering $\gamma_{\text{el-ph}}$ in more disordered cases is given in Appendix . The decrease in $\gamma_{\text{el-ph}}$ suppresses the increase in Γ at high T , resulting in higher PF in A_d than in A_p . Estimated value of l_{el} in Table I is smaller than the grain size, indicating that the PF which is mainly due to electrons is influenced by the electronic states within the grain. This is in sharp contrast to κ_{ph} as will be discussed in the section, Sec. 2.3.

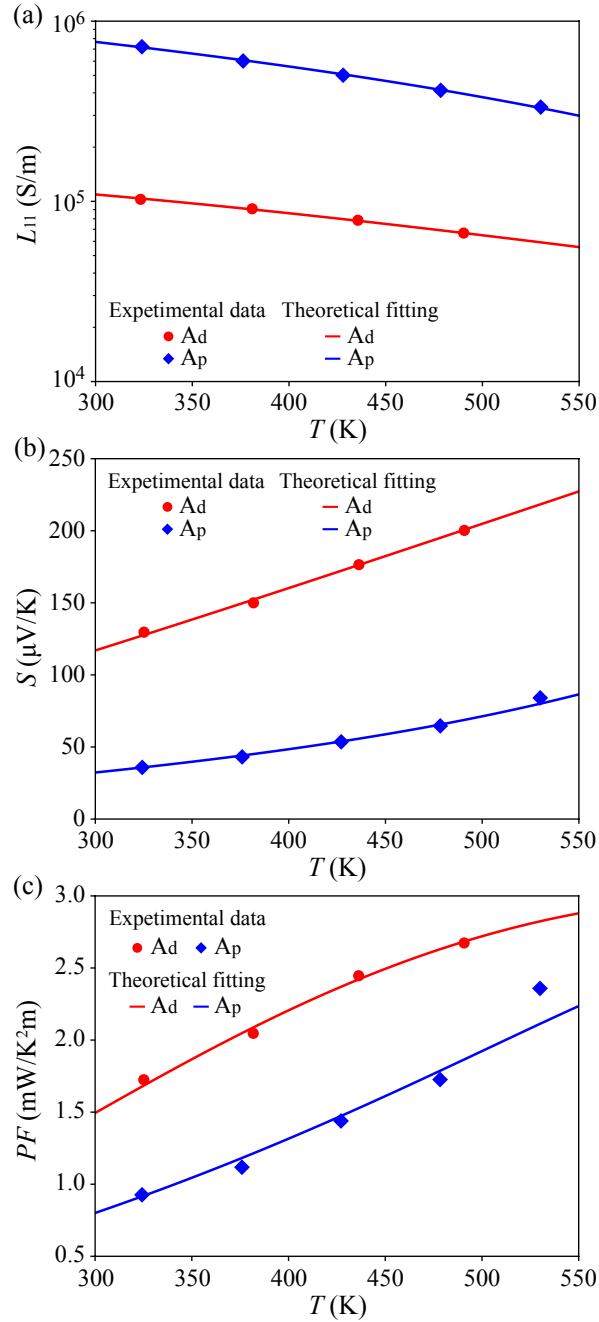


Fig. 1. (Color online) The T dependences of (a) L_{11} , (b) S , and (c) PF for pristine (A_p (blue)) and doped (A_d (red)) GeTe. The circles and squares correspond to experimental data⁶⁾ of A_p and A_d, respectively, and solid curves are results of model fitting.

With parameters obtained rather uniquely by analyzing L_{11} and L_{12} , it is possible to determine L_{22}^{el} , and then electronic contribution to ZT defined by $Z_{\text{el}}T = \frac{PE}{\kappa_{\text{el}}}T$, in terms of $\kappa_{\text{el}} = \left(L_{22}^{\text{el}} - \frac{L_{12}^2}{L_{11}}\right)\frac{1}{T}$. The $Z_{\text{el}}T$ and κ_{el} are shown as solid curves in Figs. 2(a) and 2(b), respectively, with experimental data⁶⁾ of ZT and κ for comparison. As shown in Fig. 2(a), the

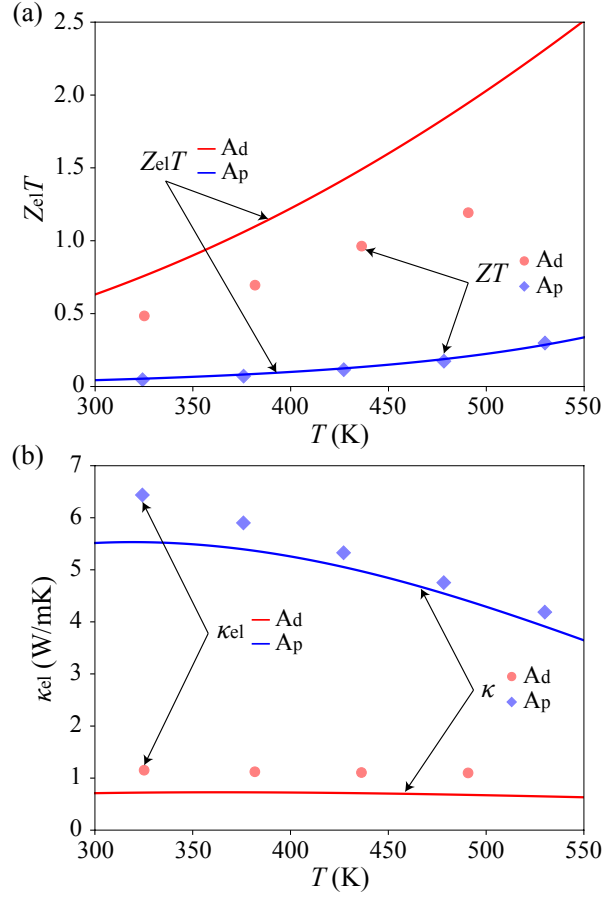


Fig. 2. (Color online) Solid curves show the T dependences of (a) $Z_{el}T$ and (b) κ_{el} for pristine (A_p (blue)) and doped (A_d (red)) GeTe, accounting only for the electron contribution, obtained from parameter fitting in Table I. The circles and squares correspond to (a) ZT and (b) κ observed in the experiment⁶⁾ for comparison.

difference between $Z_{el}T$ and ZT gives information of κ_{ph}/κ_{el} since $Z_{el}T - ZT = (\kappa_{ph}/\kappa_{el})ZT$. By using the κ_{el} determined in Fig. 2(b), it is now possible to identify κ_{ph} .

2.3 Phonon contribution to thermal conductivity; κ_{ph}

In Fig. 3, the circles and squares represent $\kappa_{ph}(= \kappa - \kappa_{el})$, in A_p and A_d, respectively. The new findings regarding magnitude and T dependences of κ_{ph} as disclosed in Fig. 3 indicate that κ_{ph} in A_d is smaller and weakly dependent on T than in A_p, which will be analyzed based on the previous studies derived for insulators.^{14–16)} (It is to be noted that extra contribution from electron-phonon scattering is present in conductors, which is ignored here.) For example, according to the Holland, κ_{ph} is given by¹⁶⁾

$$\kappa_{ph} = \frac{k_B}{2\pi^2 v} \left(\frac{k_B T}{\hbar} \right)^3 \int_0^{\theta_D/T} \frac{x^4 e^x (e^x - 1)^{-2}}{v/L + ax^4 T^4 + bx^2 T^5} dx, \quad (12)$$

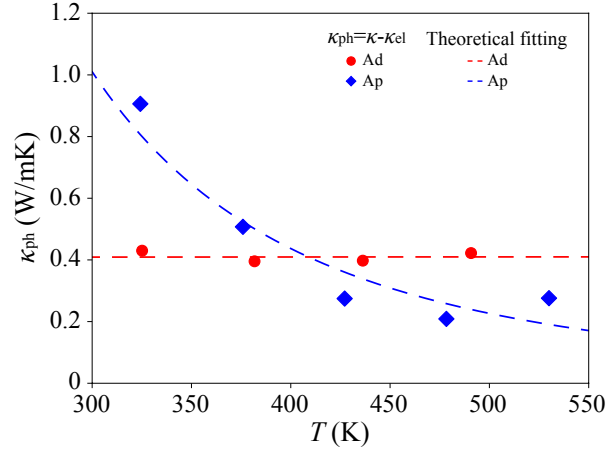


Fig. 3. (Color online) The circles and squares correspond to the T dependences of $\kappa_{\text{ph}} = \kappa - \kappa_{\text{el}}$ for pristine (A_{p} (blue)) and doped (A_{d} (red)) GeTe, respectively, and dashed curves are results of theoretical fitting based on Holland phonon thermal conductivity in Eq. (12).

where scattering by boundaries (v/L), impurities (a due to differences by mass and spring constants) and among phonons (b due to three phonons) have been taken into account. The κ_{ph} , expressed in Eq. (12), increases proportionately to T^3 at low T and decreases above the Debye temperature, θ_{D} , due to the interaction of three phonons. Dashed curves in Fig. 3 show the results of theoretical fitting of $\kappa_{\text{ph}} = \kappa - \kappa_{\text{el}}$ with L , a , and b in the Holland formula, Eq. (12). The fitting parameters listed in Table II are under the assumption that the sample size, L , is given as the average grain size in the experiment,⁶⁾ the average phonon velocity, v , is 2100 m/s, and $\theta_{\text{D}} = 199$ K, which are values in pristine GeTe.^{17,18)} It is seen that in A_{p} , v/L and b are effective, while in A_{d} with more inhomogeneity due to an increase in distribution of planar defects and smaller-sized grains, v/L is larger and a is more effective. Microscopic understanding of these interesting results between κ_{ph} and shapes/sizes of grains is beyond the scope of the present paper. On the other hand, we note that the Boltzmann type of phenomenological treatment $\kappa_{\text{ph}} = \frac{1}{3}Cv l_{\text{ph}}$, where $C(=1.5 \text{ J}/(\text{cm}^3 \text{ K})$ at 300 K¹⁹⁾) is the specific heat and l_{ph} the mean free path of phonons, results in $l_{\text{ph}}=1.0$ nm and 0.4 nm for A_{p} and A_{d} , respectively, at 300 K. Thus, l_{ph} is considerably smaller than the grain size, and also smaller than l_{el} shown in Table I, which is not physically acceptable. This unphysical result is due to the fact that the effects of a and b in Eq. (12) are not properly taken into account because of their dependences on x which are variables to be integrated.

Table II. Fitting parameters of GeTe-based compounds for κ_{ph}

	Pristine GeTe (A_p)	$\text{Ge}_{0.87}\text{Y}_{0.02}\text{Sb}_{0.10}\text{Ag}_{0.01}\text{Te}$ (A_d)
L (nm)	327.5	317.3
a ($\text{s}^{-1}\text{K}^{-4}$)	~ 0	1.24×10^5
b ($\text{s}^{-1}\text{K}^{-5}$)	5	~ 0

3. Case of Mg_3Sb_2

3.1 Electronic states and model of spectral conductivity

Mg_3Sb_2 has hexagonal crystal structure and the conduction band minima are at the CB_1 point with $g_v = 6$, which are dominated by the electronic state of the Mg atom. In the case of Mg_3Sb_2 -based compounds with Sb site substitution, $\text{Mg}_{3+\delta}\text{Sb}_{1.5}\text{Bi}_{0.49}\text{Te}_{0.01}$,⁷⁾ the electrons are doped with $m^* = 0.23m_0$ ²⁰⁾ (anisotropy of m^* is neglected). In contrast to the case of GeTe where doping effects are analyzed, we focus here on the change of thermoelectric performance by annealing in a specific sample of $\text{Mg}_{3+\delta}\text{Sb}_{1.5}\text{Bi}_{0.49}\text{Te}_{0.01}$, since they show clear and characteristic variations associated with the grains size; grain sizes $\sim 10 \mu\text{m}$ in unannealed and $> 30 \mu\text{m}$ in annealed samples. Henceforth, unannealed and annealed samples are written as B_u and B_a , respectively. From the T dependences of L_{11} in B_a showing a monotonic decrease of L_{11} with T , phonon scattering is dominant, while in B_u showing nonmonotonic T dependence, other scattering mechanisms, e.g., scattering by grain boundaries and ionized impurities, may be activated. Hence, Γ is taken as a fitting parameter to capture the feature of L_{11} by the similar scheme to $\alpha(\varepsilon)$ in Eq. (11) in the case of GeTe. Fig. 4 and Table III represent the fitting parameters Γ and μ determined to reproduce the T dependence of both L_{11} and S in the experiment.⁷⁾ As seen, Γ is proportional to T in the high- T region in accordance with expected dominance of electron-phonon scattering for both B_u and B_a , while Γ in B_u deviates from T in the low- T region due to other scattering mechanisms.

Table III. Fitting parameters of Mg_3Sb_2 -based compounds for L_{11} , S and PF , and l_{el} at $T = 300$ K

	Annealed (B_a)	Unannealed (B_u)
μ (eV)	$\varepsilon_F - 25.1 (k_B T)^2$	$\varepsilon_F - 29.4 (k_B T)^2$
ε_F (eV)	4.1×10^{-2}	4.5×10^{-2}
l_{el} (nm)	4.6	2.2

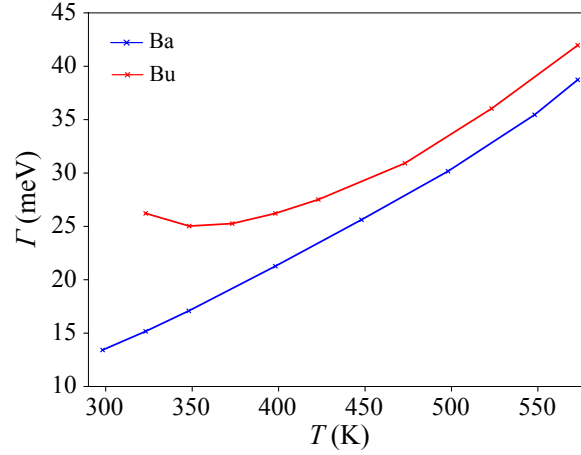


Fig. 4. (Color online) The T dependence of fitting-parameter Γ for unannealed (B_u , red) and annealed (B_a , blue) $Mg_{3+\delta}Sb_{1.5}Bi_{0.49}Te_{0.01}$.⁷⁾

3.2 Parameter-fitting for L_{11} , S , PF and electronic contributions to ZT

L_{11} , S and PF of B_u and B_a are shown in Fig. 5, where circles and squares are experimental data⁷⁾ and solid curves are model fitting with parameters given in Fig. 4 and Table III. Reflecting the Γ behavior, T dependences of both L_{11} and S become larger in the B_a , resulting in a larger PF especially at low T .

As in the case of GeTe, the electron contribution to the thermal conductivity, κ_{el} , is extracted from the results of the parameter fitting of L_{11} , S , and PF , and comparisons of the κ_{el} and $Z_{el}T$ with the actually observed κ and ZT are shown in Figs. 6(a) and 6(b), respectively. It is seen that at low T , both ZT and $Z_{el}T$ turn out to get larger by annealing.

3.3 Phonon contribution to thermal conductivity; κ_{ph}

In the case of pristine Mg_3Sb_2 , Kanno et al. indicate that κ_{ph} is proportional to T^2 at low T , and decreases moderately with T ($\kappa_{ph} \sim T^{-0.5}$) at high T .²²⁾

In the present case, κ_{ph} is shown in Fig. 7, with results of parameters fitting in κ_{ph} based on Eq. (12) given in Table IV under the assumption that L is the average grain size in the experiment,⁷⁾ $\theta_D = 208.56$ K, and $v = 2075.76$ m/s.²¹⁾ The results indicate that the effect of increasing grain size by annealing on κ_{ph} is globally minor except for the reduction of κ_{ph} at low T .

4. Comparison between GeTe and Mg_3Sb_2

Both GeTe and Mg_3Sb_2 are high ZT materials due to low κ . Comparing them, κ_{ph} is not much different, although the average grain size in GeTe is almost 2 orders of magnitude

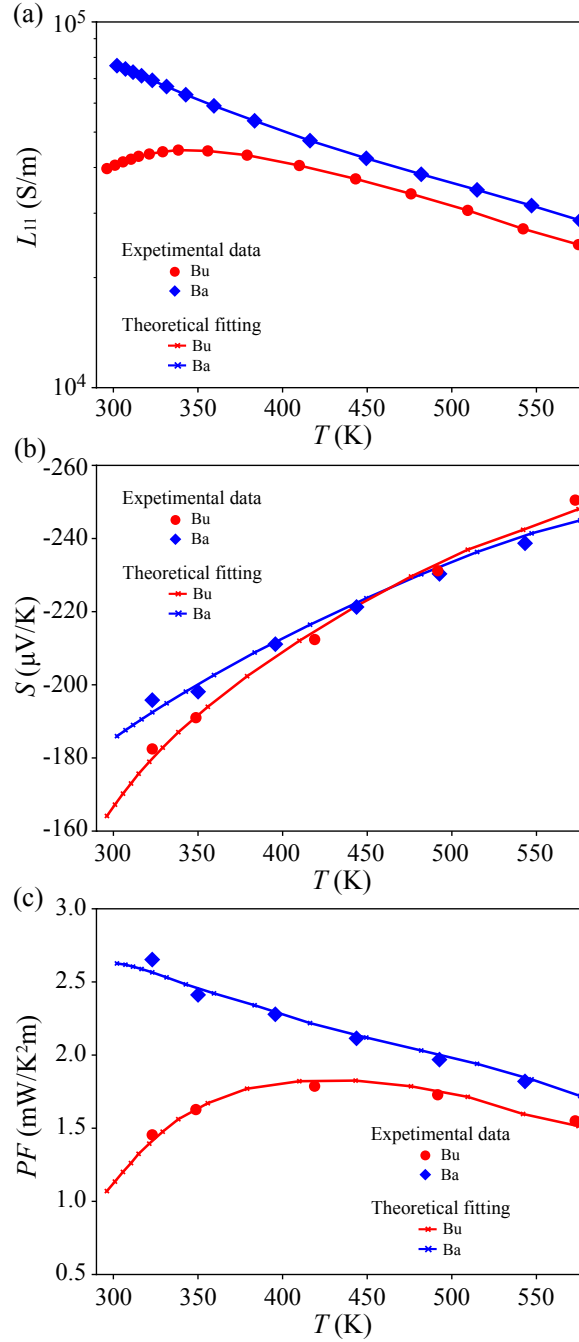


Fig. 5. (Color online) The T dependences of (a) L_{11} , (b) S , and (c) PF for unannealed (B_u (red)) and annealed (B_a (blue)) $\text{Mg}_{3+\delta}\text{Sb}_{1.5}\text{Bi}_{0.49}\text{Te}_{0.01}$. The circles and squares correspond to experimental data⁷⁾ of B_u and B_a , respectively, and solid curves are results of model fitting.

smaller than that in Mg_3Sb_2 according to experiments.^{6,7)} On the other hand, the T dependences of κ_{ph} are different for GeTe and Mg_3Sb_2 ; in the case of GeTe, the T dependence of κ_{ph} is strong for pristine GeTe (A_p) whereas weak for doped GeTe (A_d) with smaller grain size, while κ_{ph} is almost independent of grain size in the case of Mg_3Sb_2 . This difference may

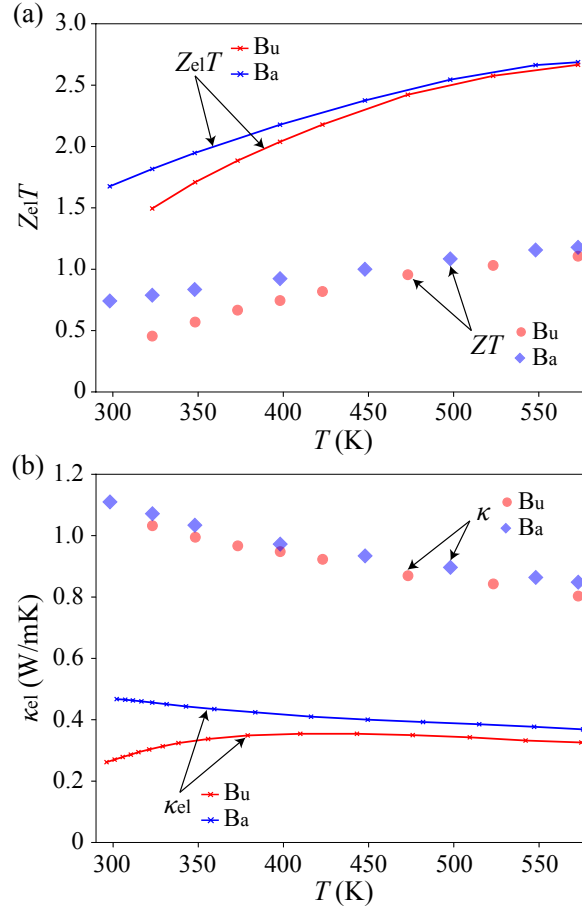


Fig. 6. (Color online) Solid curves show the T dependence of (a) $Z_{el}T$ and (b) κ_{el} , accounting only for the electron contribution, obtained from parameter fitting in Fig. 5 and Table I. The circles and squares correspond to (a) ZT and (b) κ observed in the experiment⁷⁾ for comparison.

Table IV. Fitting parameters of Mg_3Sb_2 -based compounds for κ_{ph}

	Annealed (B_a)	Unannealed (B_u)
L (μm)	30	10
a ($s^{-1}K^{-4}$)	3.28×10^5	1.64×10^5
b ($s^{-1}K^{-5}$)	0.05	0.14

be attributed to grain shapes, disrupted herringbone structure type irregular one in GeTe vs. rather uniform amorphous like one in Mg_3Sb_2 . This result indicates that it is necessary to optimize not only the sizes but also the shapes of grains to minimize κ_{ph} , leading to a higher ZT .

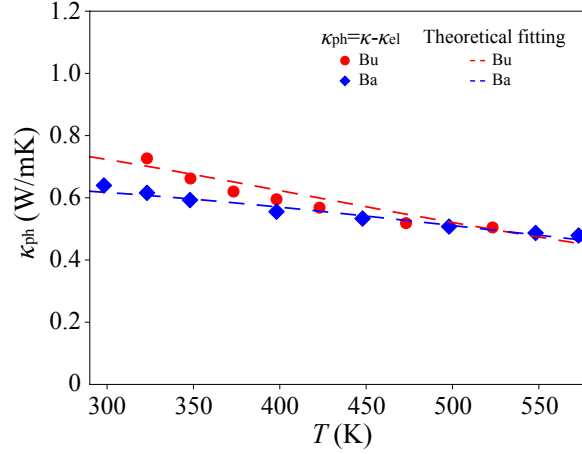


Fig. 7. (Color online) The circles and squares correspond to the T dependence of $\kappa_{\text{ph}} = \kappa - \kappa_{\text{el}}$ for unannealed (B_u (red)) and annealed (B_a (blue)) $\text{Mg}_{3+\delta}\text{Sb}_{1.5}\text{Bi}_{0.49}\text{Te}_{0.01}$, respectively, and dashed curves are theoretical fitting by Holland phonon thermal conductivity in Eq. (12).

5. Summary

The Sommerfeld-Bethe formula interrelates L_{11} (electrical conductivity), L_{12} (thermo-electric conductivity), and L_{22}^{el} (contribution of electrons to thermal conductivity) by a common physical quantity, spectral conductivity, α . In this paper we proposed that the detailed analysis of experimental data of both conductivity, L_{11} and Seebeck coefficient, $S = L_{12}/TL_{11}$, and then power factor, $PF = L_{12}L_{21}/TL_{11}$, can result in unique dependences on energy and temperature of α which in turn leads to the identification of contribution of electrons to thermal conductivity, $\kappa_{\text{el}} = L_{22}^{\text{el}} - L_{12}L_{21}/L_{11}$. By comparing experimental data of thermal conductivity, κ , governing $ZT = PF \cdot T/\kappa$, we can infer phonon thermal conductivity, $\kappa_{\text{ph}} = \kappa - \kappa_{\text{el}}$, which has been analyzed based on the formula by Holland. These results in the analysis of possible scattering mechanism by boundaries (v/L), impurities (a due to differences by mass and spring constants) and among phonons (b due to three phonons) in the formula. To the best of our knowledge, this is the first to identify various sources of T dependences of κ_{ph} .

GeTe and Mg_3Sb_2 known to exhibit high ZT are inhomogeneous with different types of crystal structures, i.e., GeTe is a disrupted herringbone structure and Mg_3Sb_2 is rather uniform amorphous. In GeTe, the T dependence of κ_{ph} is sensitive to grain size and defects, while in Mg_3Sb_2 , κ_{ph} is insensitive to grain size. This result indicates that not only size but also shapes of grains affect κ_{ph} , which deserves more systematic studies.

Based on the present results, detailed observation on sample structure and analysis of

grains patterns by, e.g. TEM and image analysis, on top of spectroscopic information, e.g. X-ray absorption or emission and photoemission spectroscopy to identify density of states (DOS) useful to construct a model of α , will be effective for further exploration of higher ZT materials.

It is of interest to extend the present analysis to $\text{Mg}_3(\text{Sb,Bi})_2$ based materials, which are expected to have practical importance as useful thermoelectrics.²⁴⁾

Acknowledgment

We thank Takao Mori(NIMS) for the fruitful discussions on experiments on GeTe.

Appendix: Effects of disorder on phonon scattering at high temperatures

Effects of phonon scattering on electrons are represented by the self-energy corrections in Fig. A-1, where solid and wavy lines are electron and phonon Green's functions, respectively. In clean systems, this process is estimated as follows,²³⁾

$$\begin{aligned}\Sigma_{\text{el-ph}}^{\text{R}}(\mathbf{k}, \varepsilon) &= -\frac{k_B T}{V} \sum_{m,q} g_q^2 \mathcal{D}(\mathbf{q}, i\omega_m) \mathcal{G}(\mathbf{k} - \mathbf{q}, i\varepsilon_n - i\omega_m)|_{i\varepsilon_n \rightarrow \varepsilon + i\delta} \\ &= -\frac{1}{V} \sum_q g_q^2 \left[\frac{f(\xi_{\mathbf{k}-\mathbf{q}}) - 1 - n(\hbar\omega_q)}{\varepsilon - \xi_{\mathbf{k}-\mathbf{q}} - \hbar\omega_q + i\delta} - \frac{f(\xi_{\mathbf{k}-\mathbf{q}}) + n(\hbar\omega_q)}{\varepsilon - \xi_{\mathbf{k}-\mathbf{q}} + \hbar\omega_q + i\delta} \right] \quad (\text{A.1})\end{aligned}$$

where $\xi_{\mathbf{k}-\mathbf{q}} = \varepsilon_{\mathbf{k}-\mathbf{q}} - \mu$, $n(\hbar\omega_q) = 1/(\exp(\beta\hbar\omega_q) - 1)$ is the Bose distribution function, and g_q is the electron-phonon coupling constant ($g_q^2 = gq$). $\mathcal{D}(\mathbf{q}, i\omega_m)$ is the phonon Green's function,

$$\mathcal{D}(\mathbf{q}, i\omega_m) = \frac{2\hbar\omega_q}{(i\omega_m)^2 - (\hbar\omega_q)^2}, \quad (\text{A.2})$$

and $\mathcal{G}(\mathbf{k} - \mathbf{q}, i\varepsilon_n - i\omega_m)$ is the free-electron Green's function,

$$\mathcal{G}(\mathbf{k} - \mathbf{q}, i\varepsilon_n - i\omega_m) = \frac{1}{i\varepsilon_n - i\omega_m - \xi_{\mathbf{k}-\mathbf{q}}}. \quad (\text{A.3})$$

The real part of $\Sigma_{\text{el-ph}}^{\text{R}}(\mathbf{k}, \varepsilon)$ leads to well-known result at $T = 0$, where $n(\hbar\omega_q) = 0$, determining the mass enhancement of electronic specific heat at low T . At high T , $k_B T \gg \hbar\omega_D$ (ω_D : Debye frequency), where $n(\hbar\omega_q) \sim k_B T / \hbar\omega_q$, the imaginary part of $\Sigma_{\text{el-ph}}^{\text{R}}(\mathbf{k}, \varepsilon)$ at $\varepsilon = 0$ leads to $-\frac{g(\hbar\omega_D)^2}{4\pi(\hbar v)^3 \hbar v_F} k_B T$ where v_F is Fermi velocity.

On the other hand in the present disordered metals, it is seen that $\Sigma_{\text{el-ph}}^{\text{R}}(\mathbf{k}, \varepsilon)$ is rewritten with electron Green's function with disorder, γ_{el} , together with phonon propagator with damping, γ_{ph} , as follows,

$$\Sigma_{\text{el-ph}}^{\text{R}}(\mathbf{k}, \varepsilon) = -\frac{k_B T}{V} \sum_{m,q} g_q^2 \frac{1}{i\varepsilon_n - i\omega_m - \xi_{\mathbf{k}-\mathbf{q}} + i\gamma_{\text{el}} \text{sign}(\varepsilon_n - \omega_m)}$$

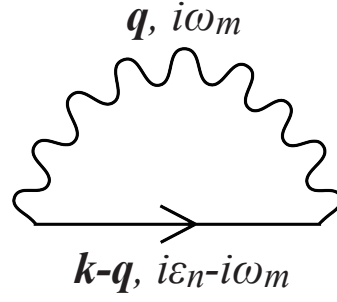


Fig. A.1. (Color online) Diagram of a self-energy for electron scattering by phonons. The wavy and solid lines respectively represent the phonon and electron.

$$\times \left(\frac{1}{i\omega_m - \hbar\omega_q + i\gamma_{\text{ph}}\text{sign}(\omega_m)} - \frac{1}{i\omega_m + \hbar\omega_q + i\gamma_{\text{ph}}\text{sign}(\omega_m)} \right) \Big|_{i\varepsilon_n \rightarrow \varepsilon + i\delta}. \quad (\text{A}\cdot 4)$$

At high T , the imaginary part of $\Sigma_{\text{el-ph}}^{\text{R}}(\mathbf{k}, \varepsilon)$ is given as

$$\text{Im}\Sigma_{\text{el-ph}}^{\text{R}}(\mathbf{k}, \varepsilon) \sim -\frac{2k_{\text{B}}T}{V} \sum_{m,q} g_q^2 \frac{\hbar\omega_q(\gamma_{\text{el}} + 2\gamma_{\text{ph}}) \{(\gamma_{\text{el}} + \gamma_{\text{ph}})^2 + \hbar^2\omega_q^2\}}{(\hbar^2\omega_q^2 + \gamma_{\text{ph}}^2) \{(\hbar\omega_q - \varepsilon + \xi_{\mathbf{k}-q})^2 + (\gamma_{\text{el}} + \gamma_{\text{ph}})^2\} \{(\hbar\omega_q + \varepsilon - \xi_{\mathbf{k}-q})^2 + (\gamma_{\text{el}} + \gamma_{\text{ph}})^2\}}, \quad (\text{A}\cdot 5)$$

and in the case that γ_{ph} and $\hbar\omega_{\text{D}}$ are smaller in strong disorder ($\gamma_{\text{el}} \gg \gamma_{\text{ph}}, \hbar\omega_{\text{D}}$), $\text{Im}\Sigma_{\text{el-ph}}^{\text{R}}(\mathbf{k}, \varepsilon)$ is written as

$$\begin{aligned} \text{Im}\Sigma_{\text{el-ph}}^{\text{R}}(\mathbf{k}, \varepsilon) &\sim -\frac{2k_{\text{B}}T}{V} \sum_{m,q} g_q^2 \frac{\hbar\omega_q}{\gamma_{\text{el}}(\hbar^2\omega_q^2 + \gamma_{\text{ph}}^2)} \\ &= -\frac{ak_{\text{B}}T}{\pi^2(\hbar v)^4\gamma_{\text{el}}} \left\{ \gamma_{\text{ph}}^3 \arctan\left(\frac{\hbar\omega_{\text{D}}}{\gamma_{\text{ph}}}\right) + \frac{(\hbar\omega_{\text{D}})^3}{3} - \gamma_{\text{ph}}^2\hbar\omega_{\text{D}} \right\}, \quad (\text{A}\cdot 6) \end{aligned}$$

where $\hbar\omega_q = \hbar vq$. Thus, γ_{el} suppresses phonon scattering, and in addition, $\text{Im}\Sigma_{\text{el-ph}}^{\text{R}}$ in dirty metals is smaller than that in clean metals at high T under the condition: $\frac{\hbar\omega_{\text{D}}}{\gamma_{\text{el}}} < \frac{3\pi}{4} \frac{v}{v_{\text{F}}}$ and $\hbar\omega_{\text{D}} \gg \gamma_{\text{ph}}$, resulting in smaller contribution of electron-phonon scattering in metals with stronger disorder.

References

- 1) R. Kubo, J. Phys. Soc. Jpn. **12**, 570 (1957).
- 2) J. M. Luttinger, Phys. Rev. **135**, A1505 (1964).
- 3) S. Shimizu, J. Shiogai, N. Takemori, S. Sakai, H. Ikeda, R. Arita, T. Nojima, A. Tsukazaki, and Y. Iwasa, Nat. Commun. **10**, 825 (2019).
- 4) M. Matsubara, T. Yamamoto, and H. Fukuyama, J. Phys. Soc. Jpn., **92**, 104704 (2023).
- 5) Y. Uematsu, T. Ishibe, T. Mano, A. Ohtake, H. T. Miyazaki, T. Kasaya, and Y. Nakamura, Nat Commun **15**, 322 (2024).
- 6) C. Liu, Z. Zhang, Y. Peng, F. Li, L. Miao, E. Nishibori, R. Chetty, X. Bai, R. Si, J. Gao, X. Wang, Y. Zhu, N. Wang, H. Wei, and T. Mori, Sci. Adv. **9**, eadh0713 (2023).
- 7) M. Wood, J. J. Kuo, K. Imasato, and G. J. Snyder, Adv. Mater., **31**, 1902337 (2019).
- 8) A. Sommerfeld, Naturwissenschaften **15**, 825 (1927).
- 9) J. Li, X. Zhang, Z. Chen, S. Lin, W. Li, J. Shen, I. T. Witting, A. Faghaninia, Y. Chen, A. Jain, L. Chen, G. J. Snyder, Y. Pei, Joule, **2**, 976 (2018).
- 10) M. Jonson and G. D. Mahan, Phys. Rev. B **21**, 4223 (1980).
- 11) M. Ogata and H. Fukuyama, J. Phys. Soc. Jpn. **88**, 074703 (2019).
- 12) T. Yamamoto and H. Fukuyama, J. Phys. Soc. Jpn. **87**, 114710 (2018)
- 13) A. Matthiessen, Rep. Br. Assoc., **32**, 144 (1862).
- 14) P G Klemens, Proc. Phys. Soc. A **68** 1113 (1955).
- 15) J. Callaway, Phys. Rev. **113**, 1046 (1959).
- 16) M. G. Holland, Phys. Rev. **132**, 2461 (1963).
- 17) L. E. Shelimova and S. K. Plachkova, Phys. Status Solidi A **104**, 679 (1987).
- 18) J. Li, Z. Chen, X. Zhang, H. Yu, Z. Wu, H. Xie, Y. Chen, and Y. Pei, Adv. Sci. **4**, 1700341 (2017).
- 19) R. Shaltaf, X. Gonze, M. Cardona, R. K. Kremer, and G. Siegle, Phys. Rev. B **79**, 075204 (2009).
- 20) J. Zhang and B. B. Iversen, J. Appl. Phys. **126**, 085104 (2019).
- 21) J. Pei, H. Li, H.-L. Zhuang, J. Dong, B. Cai, H. Hu, J.-W. Li, Y. Jiang, B. Su, L. D. Zhao, and J.-F. Li, InfoMat, **4**, e12372 (2022).
- 22) T. Kanno, H. Tamaki, M. Yoshiya, H. Uchiyama, S. Maki, M. Takata, and Y. Miyazaki, Adv. Funct. Mater., **31**, 2008469 (2021).
- 23) F. Bloch. Z. phys., **59**, 208 (1930).
- 24) S. Bano, R. Chetty, J. Babu, and T. Mori, Device, **2**, 100408 (2024).